frontiers | Frontiers in Materials

TYPE Original Research
PUBLISHED 18 March 2025
DOI 10.3389/fmats.2025.1571855

OPEN ACCESS

EDITED BY
Jiadong Qiu,
University of South China, China

REVIEWED BY
Kun Long,
Chongqing Jiaotong University, China
Yong Luo,
University of South China, China

*CORRESPONDENCE
Cheng Pan,
cpan1989@163.com

RECEIVED 06 February 2025
ACCEPTED 28 February 2025
PUBLISHED 18 March 2025

CITATION
Dai W, Gao P, Cheng B and Pan C (2025) Experimental study on the dynamic tensile behavior and energy evolution of limestone subjected to dry-wet cycles.
Front. Mater. 12:1571855.
doi: 10.3389/fmats.2025.1571855

Experimental study on the dynamic tensile behavior and energy evolution of limestone subjected to dry-wet cycles

Wusi Dai[1,2], Pengfei Gao[1,2], Bing Cheng[3] and Cheng Pan[1,3]*

[1]School of Civil Engineering and Architecture, Anhui University of Science and Technology, Huainan, China, [2]Anhui Jiangnan Chemical Industry Co., Ltd., Hefei, China, [3]Anhui Engineering Research Center of New Explosive Materials and Blasting Technology of Anhui University of Science and Technology, Huainan, China

To investigate the effects of wet-dry cycling on the dynamic tensile strength and failure characteristics of limestone, this study conducted dynamic impact loading experiments on limestone specimens subjected to varying numbers of wet-dry cycles using a Split Hopkinson Pressure Bar (SHPB) system. By integrating digital image correlation (DIC) and fractal analysis, the stress-strain evolution, crack propagation patterns, and energy dissipation mechanisms under different loading rates and wet-dry conditions were systematically analyzed. Results indicate that wet-dry cycling significantly degrades limestone's mechanical properties, reducing tensile strength and promoting complex crack propagation. Energy distribution and dissipation were also substantially influenced. While dynamic tensile strength improved with increasing loading rates, the weakening effect of wet-dry cycles became more pronounced. Additionally, interactions between main and secondary cracks grew more intricate with prolonged cycling. The fractal dimension of fragmentation increased linearly with cycle number, though sensitivity gradually declined. These findings advance the theoretical understanding of limestone failure mechanisms under coupled wet-dry cycling and dynamic loading. They also offer practical insights for mining engineering and blast design applications.

KEYWORDS

dynamic tensile behavior, dry-wet cycle, energy evolution, fractal dimension, SHPB

1 Introduction

As a predominant sedimentary rock with global distribution, limestone plays a pivotal role in engineering applications ranging from architectural construction to energy infrastructure, owing to its advantageous mechanical characteristics and geological abundance. The imperative to optimize its utilization in geotechnical engineering necessitates a comprehensive understanding of its behavioral evolution under diverse environmental stressors. Among these, cyclic dry-wet conditions emerge as a critical factor inducing progressive deterioration in strength parameters, deformation resistance, and failure mechanisms of limestone formations (Guo et al., 2021; Luo et al., 2025).

Recent advancements have elucidated the physico-mechanical degradation mechanisms in sedimentary rocks under hydric cycling. He et al. (2024) systematically examined frequency-dependent dry-wet effects on sandstone, revealing an inverse correlation between cycle numbers and uniaxial compressive strength (UCS), coupled with progressive Poisson's ratio enhancement. Studies by An et al. (2022) demonstrated hydric cycling-induced alterations in petrophysical properties, including reduced P-wave velocity alongside increased water absorption and porosity. Meng et al. (2019) established exponential decay models for key mechanical parameters (elastic modulus, secant modulus) in clay-bearing limestone under cyclic conditions, while Cai et al. (2020) employed nuclear magnetic resonance (NMR) spectroscopy to quantify irreversible porosity evolution. Fracture mechanics analyses by Hua et al. (2016) and microstructural quantification via fractal dimension modeling (Zhang et al., 2022) further corroborated the cycle-dependent deterioration hypothesis. These collective findings confirm a scientific consensus: dry-wet cycling induces progressive mechanical degradation through microstructural modification, though previous studies remain predominantly confined to quasi-static loading regimes.

The excavation of limestone mines predominantly employs drilling and blasting methods that generate high-strain-rate loading on rock masses (Gao et al., 2023; Li, 2013; Li et al., 2014; Pan et al., 2022; Qiu et al., 2023a). This engineering practice highlights a critical material vulnerability: the tensile strength of lithic materials typically constitutes merely 8%–15% of their compressive capacity, predisposing rock structures to tensile-dominated failure mechanisms under operational stresses. More critically, cyclic hydric transitions (dry-wet cycling) induce coupled petrophysical alterations and microstructural reorganization that synergistically exacerbate damage accumulation under dynamic tensile loading. Existing literature has examined the dynamics of rocks subjected to dry-wet cycles. For instance, Xu et al. (2021) quantified progressive deterioration in diorite specimens, reporting 35.6% reductions in dynamic elastic modulus and 32.5% in dynamic peak compressive strength across 8 hydric cycles, accompanied by exponential energy consumption density decrease. Similarly, Pu et al. (2024) explored the effects of dry-wet cycles on the dynamic properties and microstructure of sandstone, finding that these cycles considerably reduced its dynamic compressive strength, accelerated crack propagation, and altered its pore fractal characteristics and failure mode. Zhou et al. (2023) employed SEM/CT imaging technology to examine the progression of rock microstructures under dry-wet cyclic actions. Their observations indicated that with an increase in the number of dry-wet cycles, there was a concomitant growth in pore size and crack expansion. This resulted in a decline in both the uniaxial compressive strength and the indirect tensile strength of the specimens. Nevertheless, current understanding of energy dissipation mechanisms in cyclically weathered rocks under dynamic tensile loading remains critically incomplete. This knowledge gap significantly impedes the accurate prediction of fracture propagation patterns in practical scenarios involving coupled hygro-mechanical actions. A systematic investigation into the multiphase coupling effects between wet-dry cycling and dynamic tension–particularly focusing on crack evolution and associated energy transformation pathways–is essential for advancing fundamental fracture mechanics theory while addressing pressing engineering challenges in underground excavation and blast optimization.

This study investigates the dynamic behavior of limestone subjected to dry-wet cyclic conditions, focusing on the evolution of strain fields. Dynamic impact loading experiments were conducted on specimens after undergoing dry-wet cycle treatment, using the Split Hopkinson Pressure Bar (SHPB) testing system. The primary objective is to explore the changes in the strain field of the dry-wet cyclic rock samples. This is achieved by integrating the digital image correlation (DIC) method and analyzing the variations in energy dissipation and fractal dimension under different loading intensities and numbers of dry-wet cycles during the impact splitting process. The structure of the paper is organized as follows: Section 2 describes the experimental setup and methodology. Section 3 presents the results and analysis of the dynamic tensile behavior and energy evolution of limestone exposed to dry-wet cycles. Section 4 concludes with a summary of the key findings of this study.

2 Experimental materials and methods

2.1 Rock sample

The limestone specimens investigated in this study were obtained from the Changjiu (Shenshan) limestone mine in Anhui, China. The samples exhibited a homogeneous structure with uniform mineral particle distribution and a dark gray coloration tinged with brown. X-ray diffraction (XRD) analysis was conducted to determine the mineral composition, with results summarized in Figure 1. Quantitative analysis revealed that calcite constituted 78.20% of the total rock mass, followed by dolomite (15.20%), quartz (5.40%), and illite (1.20%).

In compliance with International Rock Dynamics Committee standards (Zhou et al., 2012), all samples were fabricated into cylindrical shapes with a diameter of 50 mm and a height of 25 mm. To ensure the integrity of the test specimens, rigorous control was implemented regarding machining precision. Specifically, the non-parallelism error between the two end faces of each specimen was required to be less than 0.05 mm, the axial deviation was not to exceed 0.25°, and the final errors in height and diameter were not to surpass 0.3 mm. Post-machining, longitudinal wave velocities were measured using a non-metallic ultrasonic flaw detector. Specimens displaying significant wave speed deviations were discarded to minimize experimental variability.

2.2 Drying-wetting procedure

The dry-wet cycling protocol followed the methodology of Khanlari and Abdilor (2015). Each cycle consisted of two phases: Initially, specimens were fully submerged in water at 20°C ± 3°C for 24 h using stainless steel mesh supports, maintaining a 20 mm water level above sample surfaces. Subsequently, the specimens are transferred to an oven and dried at 105°C for 24 h, as illustrated in Figure 2. Post-drying, samples were immediately placed in a desiccator containing silica gel and cooled to room temperature (25°C ± 2°C) for 2 h to eliminate residual thermal stresses. Temperature and humidity during cooling were monitored

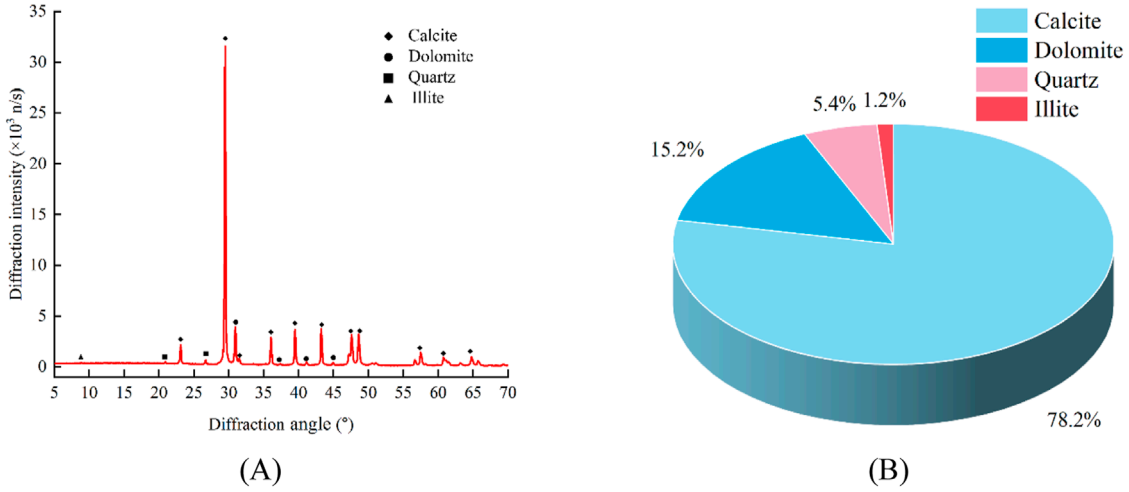

FIGURE 1
XRD analysis and mineral composition **(A)** Diffraction spectrum of limestone, **(B)** Mineral content distribution.

FIGURE 2
Dry-wet cycle treatment **(A)** Water immersion setup, **(B)** Oven-drying configuration.

using a calibrated hygrometer (accuracy: ±1°C, ±3% RH). Prior to initial testing, all specimens underwent 12 h of pre-drying at 60°C to standardize initial moisture content (0.5% ± 0.1%, measured via gravimetric analysis). Six dry-wet cycle regimes (0, 1, 5, 10, 15, and 20 cycles) were implemented to evaluate their impact on limestone properties.

2.3 Dynamic impact testing

Dynamic impact tests were conducted using a Split Hopkinson Pressure Bar (SHPB) system (Figure 3), which consists of a loading actuator, energy absorption components, compression bars, and a signal acquisition/data processing unit. The system employed high-strength alloy steel components (Young's modulus: 210 GPa, density: 7,800 kg/m^3) with standardized dimensions: the bullet is Ø50 mm × 600 mm, the incident/transmission bars are Ø50 mm × 2,500 mm, and the absorption bar is Ø50 mm × 1,500 mm.

The SHPB methodology relies on the principles of one-dimensional stress wave propagation and uniform stress distribution (Pan et al., 2025). To ensure stress equilibrium prior to specimen failure, the relationship between incident (ε_I), reflected (ε_R), and transmitted (ε_T) waves must satisfy Equation 1 (Li et al., 2017; Qiu et al., 2023b):

$$\varepsilon_I(t) + \varepsilon_R(t) = \varepsilon_T(t) \tag{1}$$

During experimental execution, vacuum mud was applied to shape the incident waveform at the end of the incident bar, while Vaseline lubrication at the rock-bar interface minimized end-face friction effects. To ensure SHPB result validity, stress equilibrium in the specimen was required prior to failure. Figure 4 illustrates the dynamic stress outcomes of a representative specimen, demonstrating close alignment between the transmitted wave stress curve and the superimposed incident/reflected waves. This congruence confirms balanced stress distribution across the specimen before failure, thereby validating the experimental methodology.

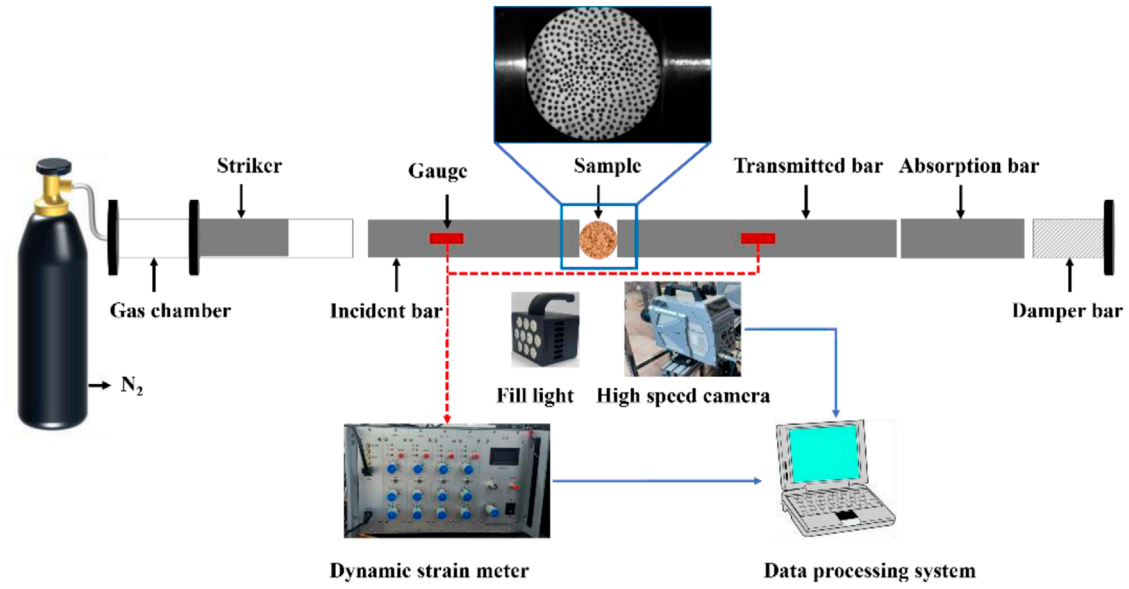

FIGURE 3
SHPB experimental setup with high-speed digital test system.

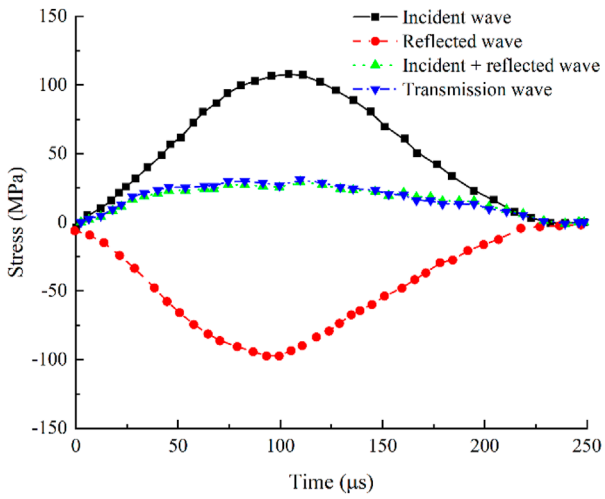

FIGURE 4
Stress equilibrium validation during dynamic loading.

For Brazilian disc tensile testing, dynamic tensile stress (σ_t) at the specimen center was calculated using Equation 2 as follows:

$$\sigma_t = \frac{2P}{\pi t d} \tag{2}$$

where P represents the effective load applied to both ends of the rock sample, t denotes the sample thickness, and d corresponds to the sample diameter. Figure 5 illustrates the dynamic tensile loading configuration. The effective load P acting on the bar ends, as expressed in Equation 3, is given by:

$$P = \frac{P_1 + P_2}{2} = \frac{AE(\varepsilon_I + \varepsilon_R) + AE\varepsilon_T}{2} = AE\varepsilon_T \tag{3}$$

yields the dynamic tensile stress equation, as given in Equation 4:

$$\sigma_t = \frac{2AE\varepsilon_T}{\pi t d} \tag{4}$$

where E denotes rod elastic modulus, A represents cross-sectional area.

2.4 Determination of loading rate

During SHPB testing, bullet velocity was regulated by adjusting impact air pressure to establish controlled loading rates. Impact pressures of 0.15, 0.20, 0.25, and 0.30 MPa were employed in this study. As shown in Figure 6, the limestone specimen exhibits a characteristic stress-time curve during dynamic tensile loading. Prior to reaching peak stress, the stress-time relationship displays near-linear behavior. The loading rate ($\dot{\sigma}$) was calculated as the slope of this linear region to quantify dynamic loading conditions.

3 Experimental results and analysis

3.1 Stress-time curve analysis

Figure 7 presents the stress-time curves of limestone specimens (0 dry-wet cycles, n = 0) under varying loading rates, revealing three key trends. First, tensile peak stress exhibits a proportional relationship with loading rate, increasing by approximately 37.6% when the loading rate is elevated from 546.71 to 954.19 GPa·s^{-1}. Specifically, when the loading rates are 546.71 GPa·s^{-1}, 721.56 GPa·s^{-1}, 876.01 GPa·s^{-1}, and 954.19 GPa·s^{-1}, the dynamic tensile strength peaks are 9.66 MPa,

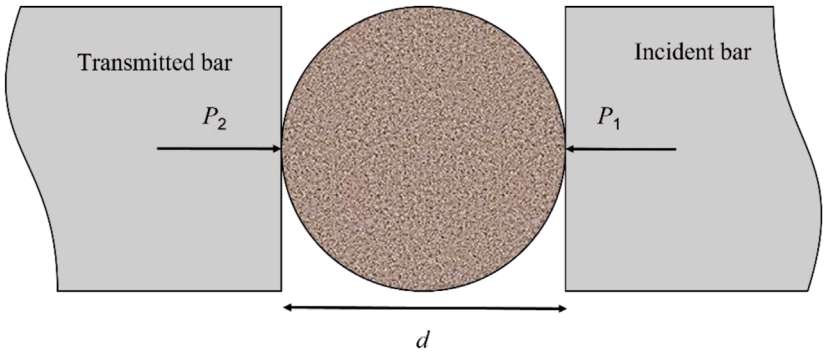

FIGURE 5
Dynamic tensile loading schematic for Brazilian disc test.

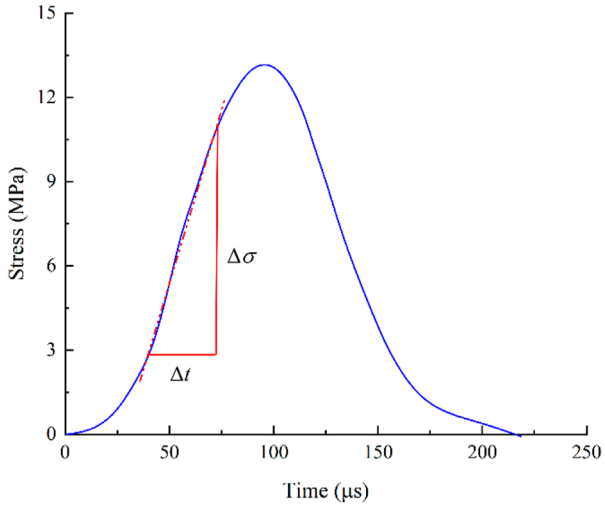

FIGURE 6
Measured tensile stress curve.

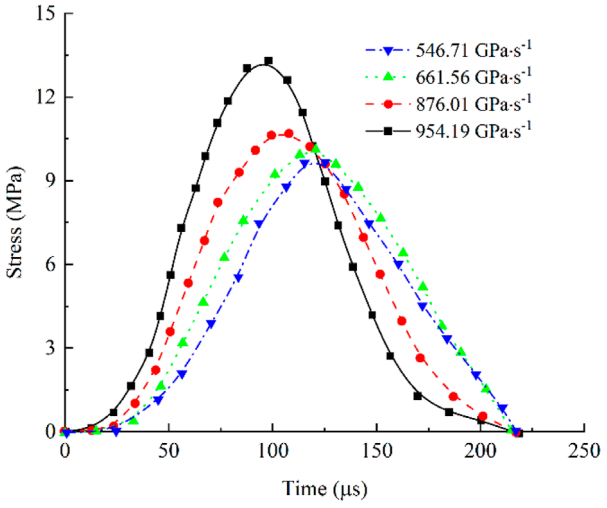

FIGURE 7
Stress-time curves of specimens subjected to varying loading rates under 0 dry-wet cycles.

10.12 MPa, 12.24 MPa, and 13.30 MPa, respectively. Second, higher loading rates significantly shorten the time to peak stress, with a reduction of 16%–27% compared to lower rates. The stress evolution follows a two-stage pattern: during the initial phase, pre-existing cracks undergo compressive closure, resulting in slower stress accumulation, followed by a rapid stress escalation phase until peak stress is attained. Following failure, stress decays abruptly, dropping to 10%–20% of peak values within 0.082 ms, a behavior consistent with limestone's inherent brittleness that drives instantaneous structural collapse upon reaching critical stress thresholds. These observations underscore the dual influence of loading rate on both dynamic strength enhancement and accelerated failure mechanisms in pristine limestone specimens.

Figure 8 compares stress-time histories of specimens exposed to identical dynamic loading (1,000 GPa·s^{-1}) but differing dry-wet cycles. Results demonstrate a systematic reduction in peak stress with increasing cycle count-specimens subjected to 20 cycles exhibit a 22.1% lower peak stress compared to untreated samples. Concurrently, the time to peak stress increases by 15.6% for cycled specimens, attributed to progressive damage from hydration-dehydration processes. Cyclic wetting-drying propagates pre-existing microcracks, weakens intergranular bonds, and elevates porosity, collectively delaying stress accumulation.

Figure 9 quantifies the loading rate dependence of tensile strength, revealing a robust linear correlation (R^2 = 0.96) between peak stress and loading rate. At 1,000 GPa·s^{-1}, peak stresses for 0, 1, 5, 10, 15, and 20 cycles correspond to 3.51, 3.39, 3.43, 3.42, 3.41, and 3.33 times static strength, respectively. While higher loading rates enhance tensile strength, increased dry-wet cycling

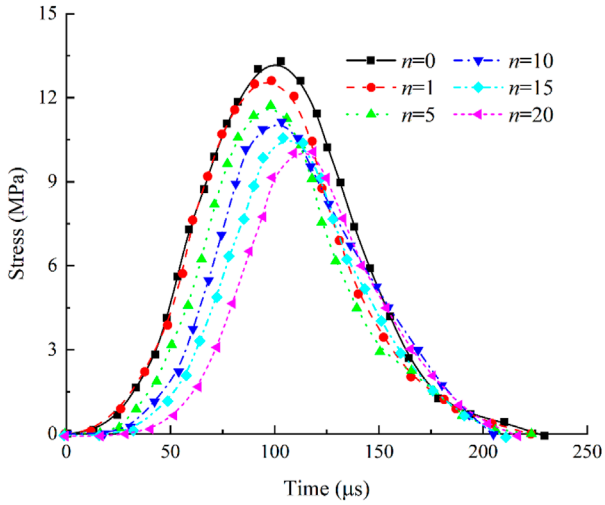

FIGURE 8
Stress-time curves of specimens under different dry-wet cycles (1,000 GPa·s^{-1}).

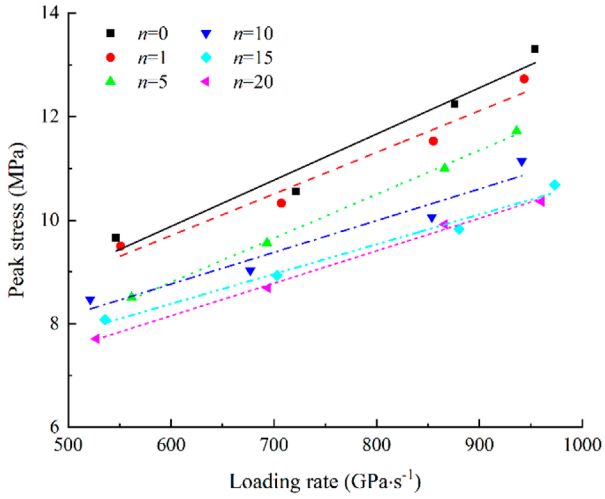

FIGURE 9
Peak tensile stress at different loading rates.

reduces rate sensitivity by 29.2%, as quantified by the slope coefficient k in the linear fit $\sigma_t = \sigma_0 + k\dot{\sigma}$ (Equation 5). This dual trend highlights the competing effects of strain rate hardening and cyclic weathering-induced degradation on limestone's mechanical behavior.

$$\begin{cases} \sigma_t = 4.526 + 0.0089\dot{\sigma} & R^2 = 0.960 \quad (n = 0) \\ \sigma_t = 4.879 + 0.0080\dot{\sigma} & R^2 = 0.984 \quad (n = 1) \\ \sigma_t = 3.702 + 0.0085\dot{\sigma} & R^2 = 0.998 \quad (n = 5) \\ \sigma_t = 5.088 + 0.0061\dot{\sigma} & R^2 = 0.972 \quad (n = 10) \\ \sigma_t = 4.932 + 0.0057\dot{\sigma} & R^2 = 0.985 \quad (n = 15) \\ \sigma_t = 4.387 + 0.0063\dot{\sigma} & R^2 = 0.998\text{b} \quad (n = 20) \end{cases} \tag{5}$$

3.2 Deformation and failure process analysis

3.2.1 Evolution characteristics of strain field

This study employed a high-speed camera to document the dynamic splitting process of limestone under various loading rates during dry-wet cycles, continuously capturing digital images. The initial speckle pattern of the limestone sample, prior to impact loading, served as a reference. The Gom Correlate digital image post-processing software (Jorge et al., 2022) was utilized to analyze and compute the dynamic changes in the speckle images throughout the loading process. This analysis facilitated the identification of variation patterns in the strain field of the limestone, influenced by dry-wet cycles and loading rates.

Figure 10 captures the temporal evolution of strain fields in dynamically split limestone specimens. The analysis defines the stress-stable initial state as the temporal reference (0 μs, Figure 10A). Upon incident wave impingement, strain localization initiates at the specimen center (Figure 10B), propagating radially toward the loading contact points along the diametral axis. This central strain concentration arises from two synergistic mechanisms: (1) microstructural inertia: under high-rate loading, heterogeneous grain boundaries (e.g., calcite-quartz interfaces) impede uniform deformation, inducing localized stress intensification; (2) dynamic stress amplification: wave reflection at free surfaces generates tensile stress doubling, exceeding the local strength threshold. The high-strain zone expands radially (Figures 10C, D) as stored elastic energy drives crack nucleation at 105 μs. By 120 μs, the high-strain region enlarges significantly as the crack penetrates the specimen, widening continuously until catastrophic splitting occurs. Post-failure stages (Figures 10E-H) exhibit secondary strain concentrations at specimen edges due to residual impact energy, accompanied by crack width amplification exceeding the digital image correlation (DIC) measurement threshold. Concurrent secondary crack formation demonstrates bifurcation tendencies toward the primary fracture, with crack network coalescence ultimately defining the failure surface morphology.

Given that macroscopic crack formation triggers specimen instability accompanied by deformation exceeding DIC measurement thresholds, this analysis focuses exclusively on pre-failure strain field evolution. Figure 11 delineates the progression of maximum principal strain in untreated specimens (n = 0) under varying loading rates. Upon incident wave impingement, strain localization initiates at the specimen center, propagating bidirectionally along the diametral axis toward the pressure rod contact points. A well-defined strain concentration band emerges centrally, expanding radially with prolonged loading. At 120 μs, maximum principal strain magnitudes reach 4.07, 4.46, 4.73, and 5.15 under 0.15, 0.20, 0.25, and 0.30 MPa impact pressures, respectively, demonstrating a positive correlation between strain intensity and loading rate. Higher loading pressures accelerate strain accumulation rates, enabling rapid development of penetrating strain bands at the specimen core. Concurrently, secondary strain localization forms at rod-specimen interfaces, establishing precursor zones for macroscopic fracture initiation. These observations

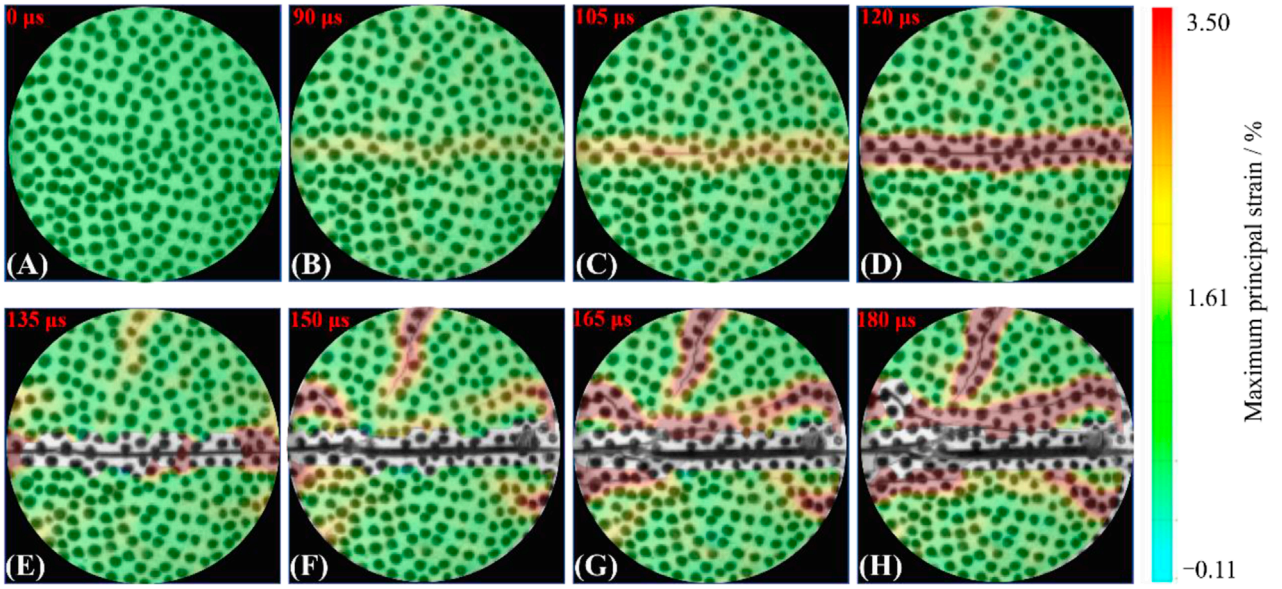

FIGURE 10
Evolution process of typical strain field at different times **(A)** 0 μs, **(B)** 90 μs, **(C)** 105 μs, **(D)** 120 μs, **(E)** 135 μs, **(F)** 150 μs, **(G)** 165 μs, **(H)** 180 μs.

collectively highlight the synergistic relationship between dynamic loading intensity and strain localization patterns preceding catastrophic failure.

Figure 12 presents the dynamic tensile strain field evolution of limestone specimens under 0.15 MPa impact pressure with varying dry-wet cycle counts. Irrespective of cycle number, strain localization initiates at the specimen center upon impact loading, forming a maximum principal strain concentration zone that propagates radially outward. Progressive loading expands this zone until catastrophic failure occurs. The strain field maintains notable symmetry, with peak tensile strain persistently localized at the central region. At equivalent loading rates, specimens subjected to increased dry-wet cycles exhibit both enlarged strain concentration zones and elevated maximum principal strain values (Figures 12A–F). The amplified strain localization and crack complexity in cycled specimens arise from cyclic hydration-induced degradation. Repeated water infiltration dissolves calcite cementation at grain boundaries, while drying generates capillary stresses that widen pre-existing microcracks. This dual process weakens intergranular cohesion, lowering the energy barrier for crack initiation. Consequently, even under identical loading rates, dry-wet cycled specimens exhibit earlier crack nucleation and accelerated propagation velocities compared to untreated samples.

3.2.2 Evolution characteristics of dynamic fracture

The evolution of crack propagation under impact loading provides critical insights into energy dissipation and dynamic failure mechanisms. In this study, crack development was analyzed using ImageJ software (Rueden et al., 2017), where the fracture network was processed through extraction and binarization to quantify crack-related pixel data. This methodology enabled precise measurement of primary crack widths at successive time intervals, with maximum crack propagation widths annotated within the imagery to track fracture dynamics.

Figure 13 delineates crack propagation dynamics in untreated limestone specimens (n = 0) under varying loading rates. Upon incident wave loading, strain localization at the specimen center initiates primary tensile crack formation, driving splitting failure. Post-primary crack nucleation, stress redistribution propagates toward the specimen ends, inducing oblique secondary cracks at the periphery of the strain concentration zone. Temporal analysis reveals progressive crack expansion and elongation, with primary and secondary fractures coalescing at 180 μs to complete structural failure. Crack aperture widths exhibit loading pressure dependence, increasing from 5.74 mm at 0.15 MPa to 7.41 mm at 0.30 MPa, correlating with accelerated propagation kinetics. Enhanced loading pressure further activates stress-induced microcracking near the primary fracture, contributing to strain-rate hardening and amplifying the specimen's apparent strength. This microcrack-mediated strengthening mechanism underscores limestone's heightened sensitivity to loading rate variations under dynamic conditions. Specifically, at the microscopic level, the interaction between primary and secondary cracks is a crucial aspect of the crack network formation. Primary cracks, once initiated, create stress concentrations at their tips, which can lead to the nucleation of secondary cracks. As these secondary cracks propagate, they may merge with the primary crack or with other secondary cracks, forming a more interconnected fracture network. This merging process is influenced by factors such as the angle between the cracks, the local stress field, and the material properties of the limestone. The formation and coalescence of these

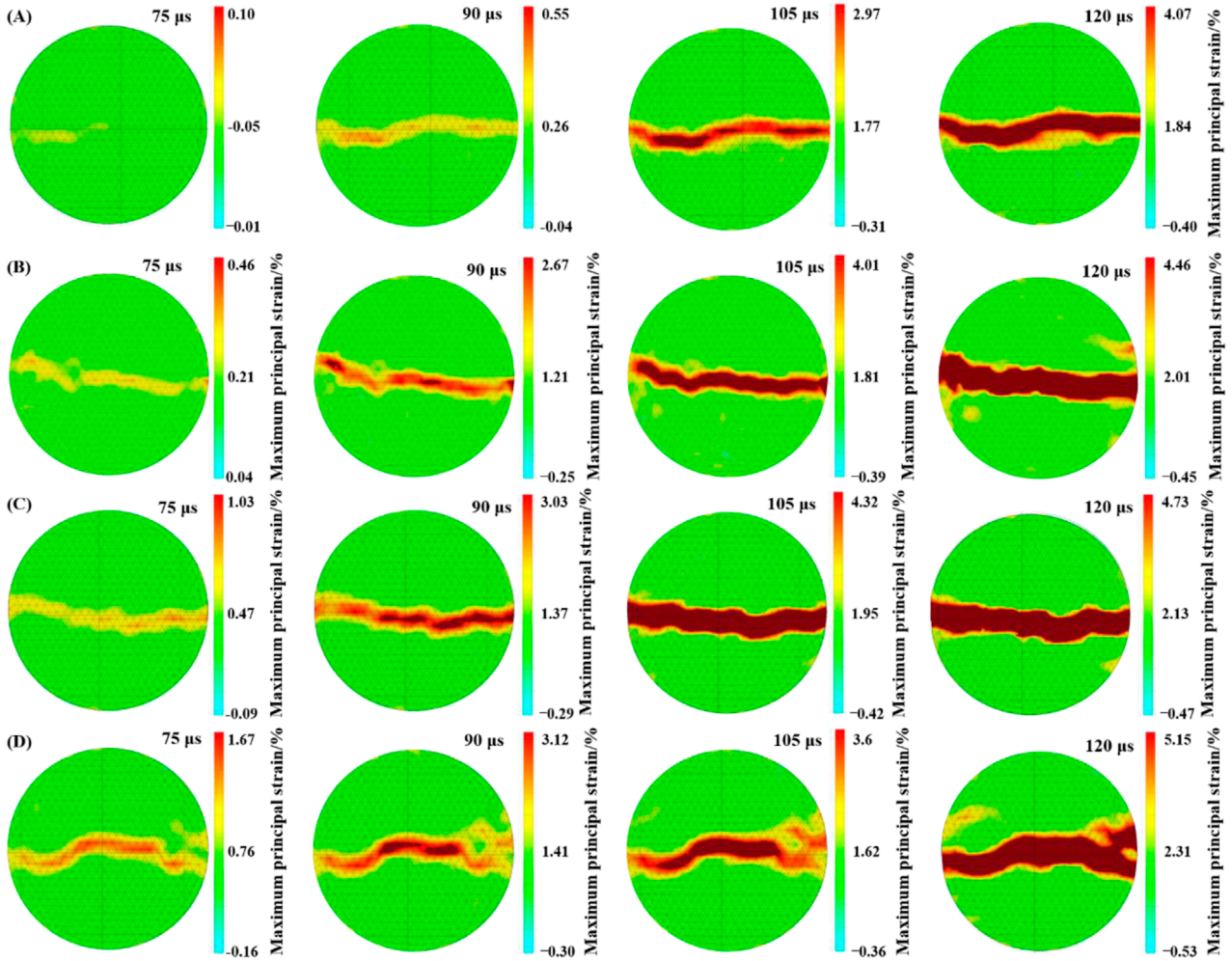

FIGURE 11
Maximum principal strain distribution of limestone under different pressure loading (n = 0) **(A)** 0.15 MPa, **(B)** 0.20 MPa, **(C)** 0.25 MPa, **(D)** 0.30 MPa.

microcracks contribute to the overall fracture pattern observed in the specimens.

Figure 14 captures the dynamic failure progression of limestone specimens under 0.30 MPa impact loading with varying dry-wet cycles. Across all tested cycles, crack propagation follows a consistent sequence: primary tensile cracks initiate centrally along the loading axis (Figures 14A–C), widening progressively while interacting with obliquely oriented secondary cracks. Compared to untreated specimens (0 cycles), cycled samples exhibit heightened damage complexity, with secondary crack density increasing and fragmentation severity rising proportionally to cycle count. Cyclic hydration-dehydration preferentially weakens intergranular bonds, enabling secondary cracks to propagate along pre-damaged microstructural planes adjacent to primary fractures. Post-coalescence, these fracture networks evolve into continuous failure surfaces (Figures 14D–F), while peripheral secondary cracks display reduced apertures, confirming stress dissipation from the core. Notably, specimens with ≥10 cycles develop compressive failure zones at loading boundaries, expanding cyclically weakened regions by 1.4%–39.0% compared to pristine samples. This dual tension-compression failure mechanism underscores how dry-wet cycling amplifies stress concentration effects, accelerating both crack nucleation kinetics and macroscopic fracture complexity under dynamic loading.

3.3 Dynamic tensile energy dissipation analysis

Energy serves as the fundamental driver of material failure, governing both deformation and fracture processes. Analyzing energy evolution during dynamic rock failure provides critical insights into how cyclic hydration-dehydration alters limestone's fracturing behavior and fragmentation patterns. In dynamic splitting tests, the energy components of incident (W_I), reflected (W_R), and transmitted (W_T) waves are quantified using one-

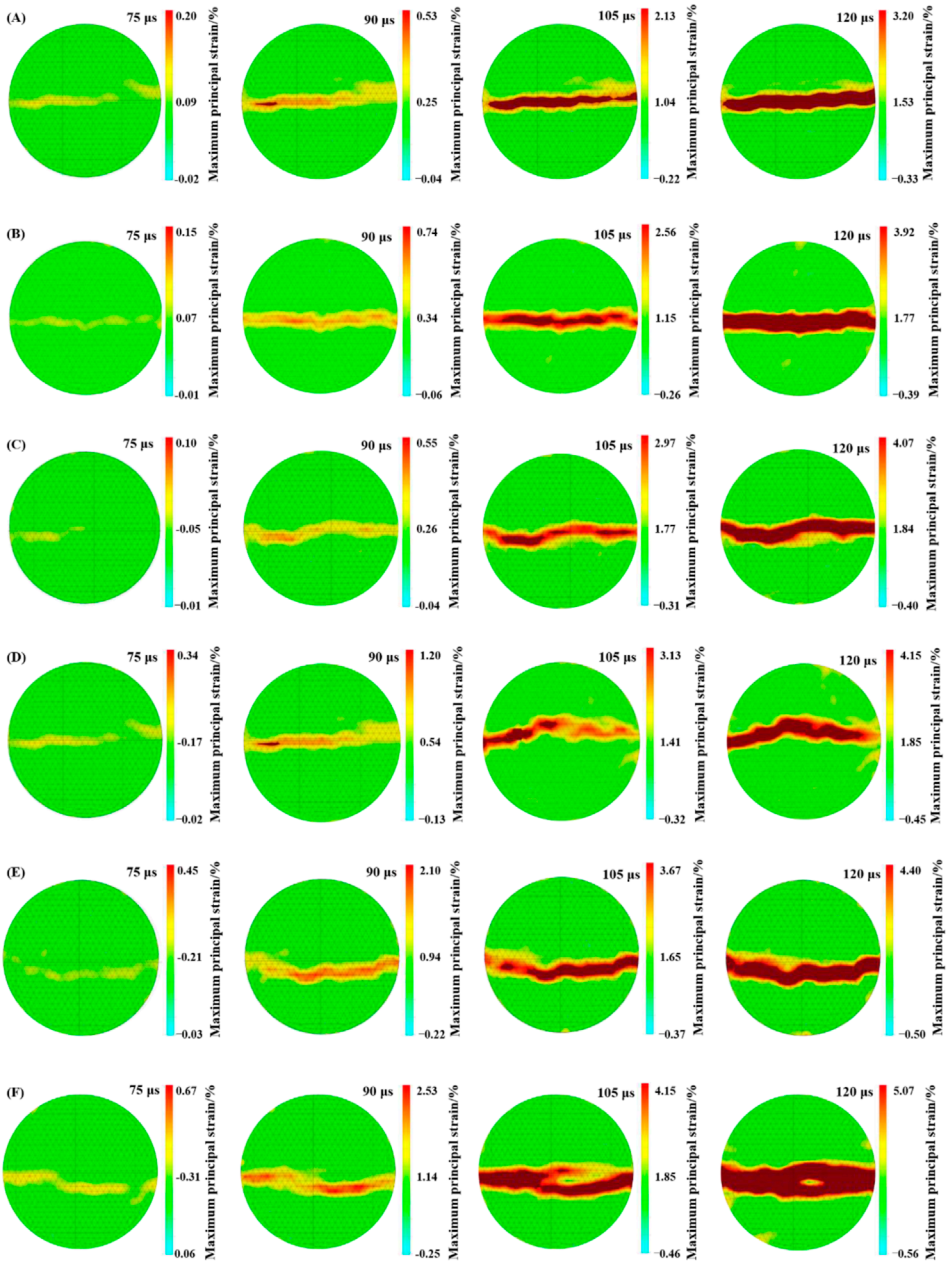

FIGURE 12
Evolution of maximum principal strain distribution in limestone under 0.15 MPa impact pressure with increasing dry-wet cycles **(A)** n = 0, **(B)** n = 1, **(C)** n = 5, **(D)** n = 10, **(E)** n = 15, **(F)** n = 20.

dimensional elastic wave theory (Zhou et al., 2023). The energy components are given by Equation 6:

$$\begin{cases} W_I = AEC_0 \int_0^t \varepsilon_i^2(t)dt \\ W_R = AEC_0 \int_0^t \varepsilon_r^2(t)dt \\ W_T = AEC_0 \int_0^t \varepsilon_t^2(t)dt \end{cases} \tag{6}$$

where A is the cross-sectional area, C_0 denotes the elastic wave velocity, and E represents the elastic modulus.

The energy dissipated during rock fracture and fragmentation under impact loading is quantified by Equation 7 (Zhou et al., 2023):

$$W_S = W_I - W_R - W_T \tag{7}$$

To mitigate specimen size effects, dissipated energy density is introduced and calculated using Equation 8:

$$\xi_S = \frac{W_S}{V} \tag{8}$$

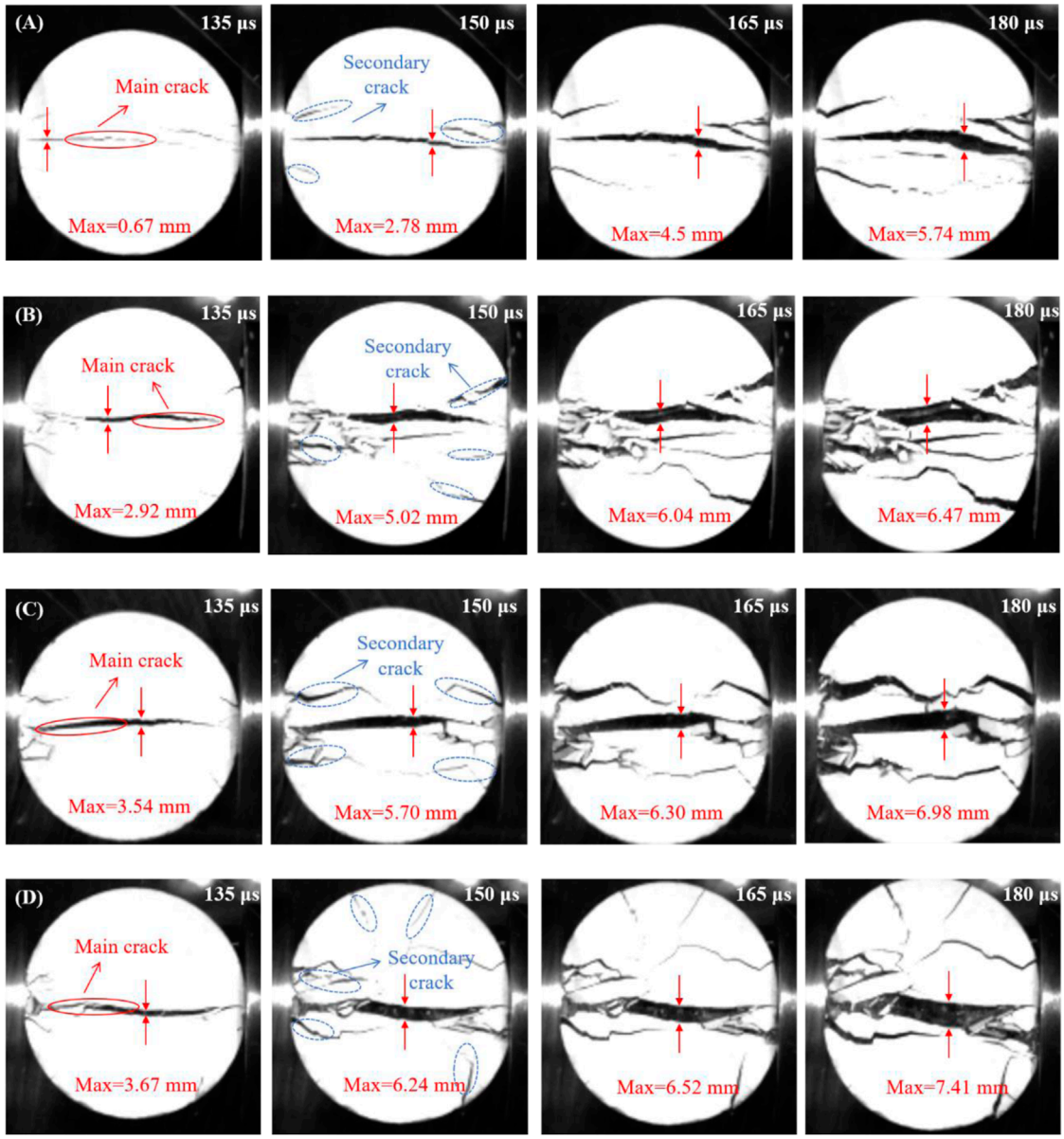

FIGURE 13
Dynamic splitting crack propagation of samples under different loading pressures (n = 0) **(A)** 0.15 MPa, **(B)** 0.20 MPa **(C)** 0.25 MPa, **(D)** 0.30 MPa.

Here, V denotes the specimen volume (cm^3). Energy utilization efficiency (η), which characterizes the rock's capacity to absorb energy, is defined by Equation 9:

$$\eta = \frac{W_S}{W_I} \tag{9}$$

Figure 15 delineates the interplay between energy components, dry-wet cycles, and loading rates. Under increasing loading rates (550–1,000 GPa·s^{-1}), incident energy escalates from 48.25 J to 102.59 J (2.13 times), while reflected and transmitted energies rise to 44.85 J (1.92 times) and 17.26 J (2.05 times), respectively (Figure 15A). Dissipated energy exhibits the most pronounced growth, surging from 16.45 J to 40.48 J (2.46 times), highlighting its dominance in dynamic fracture processes. At constant loading rates, cyclic hydration-dehydration alters energy partitioning: reflected energy increases by 33% (44.85 J–59.77 J) across 0–20 cycles, while dissipated and transmitted energies decline by 33.8% and 15.1%, respectively (Figure 15B). This redistribution stems from dry-wet-induced reductions in limestone's wave impedance, which amplifies wave reflection and attenuates transmission. Concurrently, cyclic damage degrades load-bearing capacity, lowering energy absorption thresholds and diminishing dissipated energy. The divergent trends underscore how environmental cycling exacerbates energy reflection while suppressing energy dissipation, critically influencing failure energetics under dynamic loading.

Figure 16 delineates the relationship between energy utilization efficiency (η) and loading rate for limestone specimens under varying dry-wet cycles. As shown in Figure 16A, η exhibits a linear increase with loading rate, rising from 34.1% at 550 GPa·s^{-1} to 39.5% at 1,000 GPa·s^{-1}. At lower rates, minimal crack initiation allows

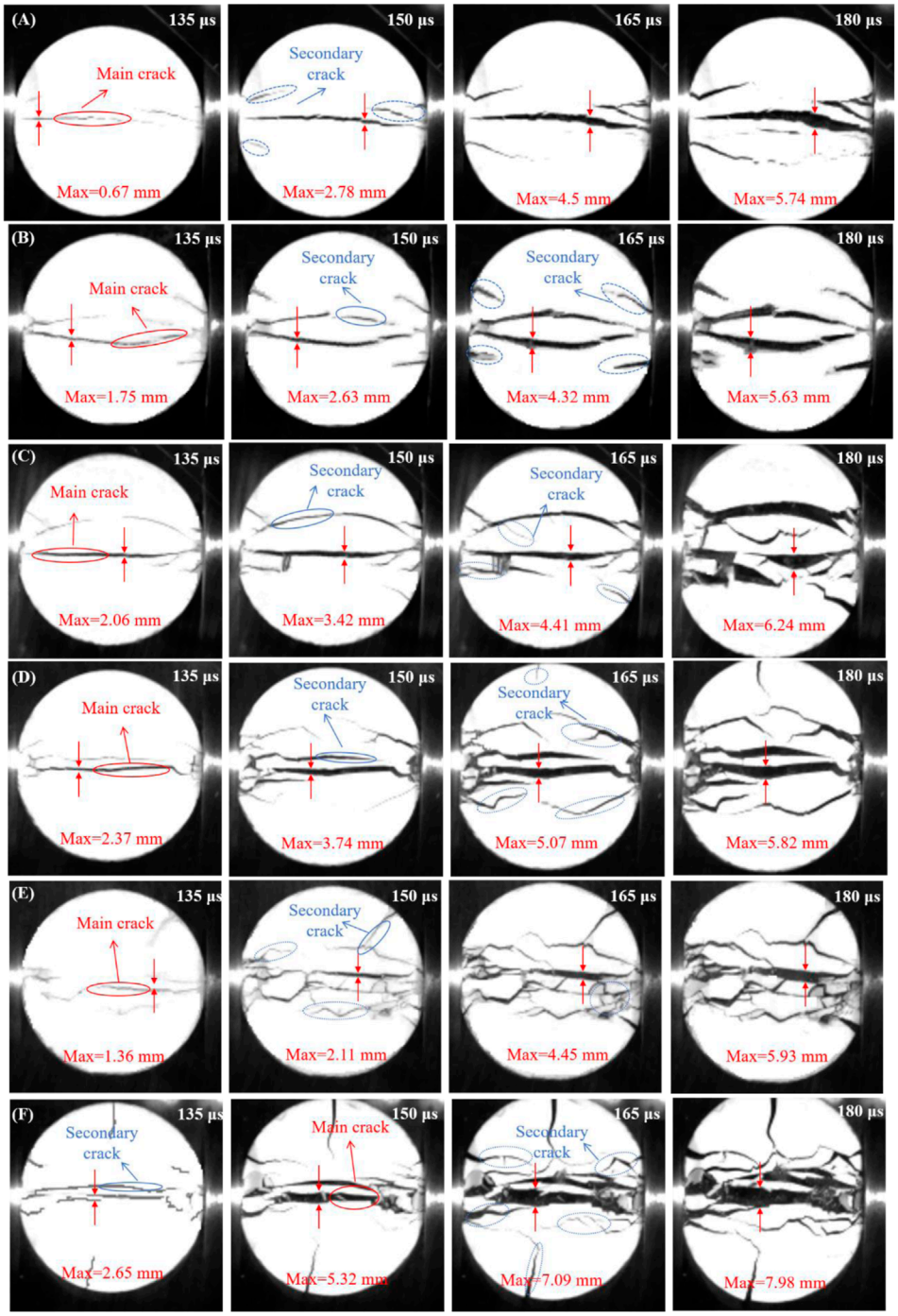

FIGURE 14
Dynamic splitting crack propagation process of samples under different dry-wet cycles (0.30 Mpa) **(A)** n = 0, **(B)** n = 1, **(C)** n = 5, **(D)** n = 10, **(E)** n = 15, **(F)** n = 20.

significant energy reflection/transmission, limiting dissipation. Higher loading rates (e.g., >850 GPa·s^{-1}) promote dynamic fragmentation, amplifying dissipated energy by 31.2%–37.1% through intensified crack propagation. Figure 16B reveals a progressive decline in η with dry-wet cycles–efficiency drops from 39.5% (0 cycles) to 31.9% (20 cycles), a 19.2% reduction. Cyclic hydration-dehydration degrades intergranular cohesion, reducing deformation resistance and lowering the energy absorption threshold by 17%. This microstructural weakening shifts energy partitioning toward reflection (increasing by 33% at n = 20) while suppressing dissipation, ultimately diminishing the specimen's capacity to utilize energy for fracture processes. The antagonistic effects of strain-rate hardening and cyclic damage highlight the dual dependence of energy efficiency on both dynamic loading

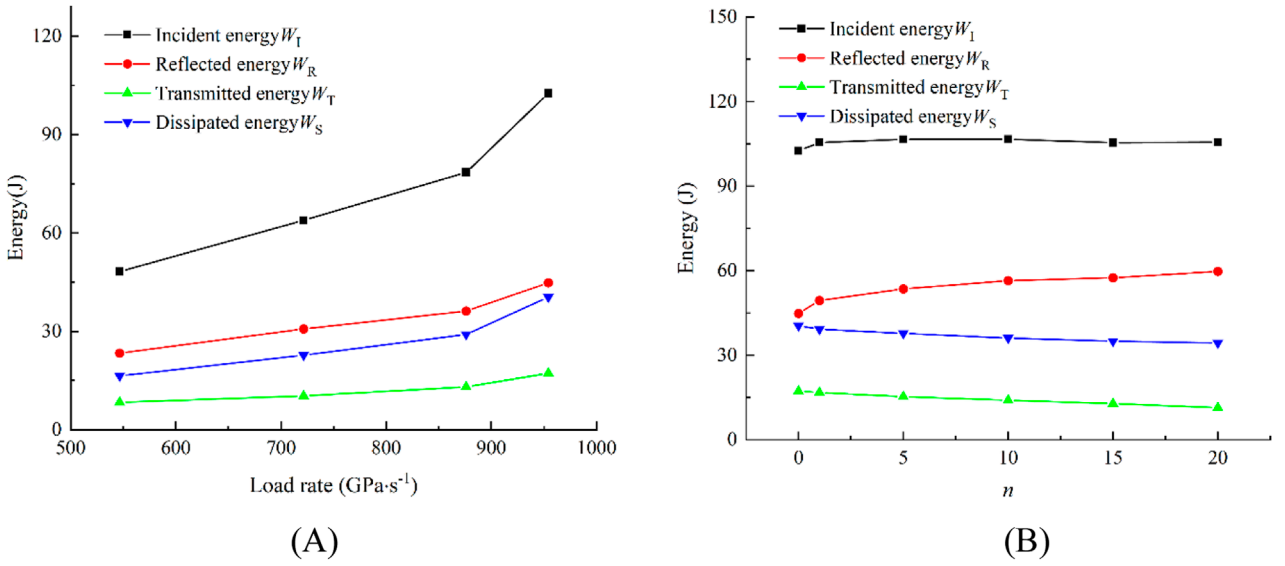

FIGURE 15
The variation law of each energy in the dynamic splitting process **(A)** Change of energy with loading rate (n = 0), **(B)** The change of energy with the number of dry and wet cycles (1,000 GPa·s^{-1}).

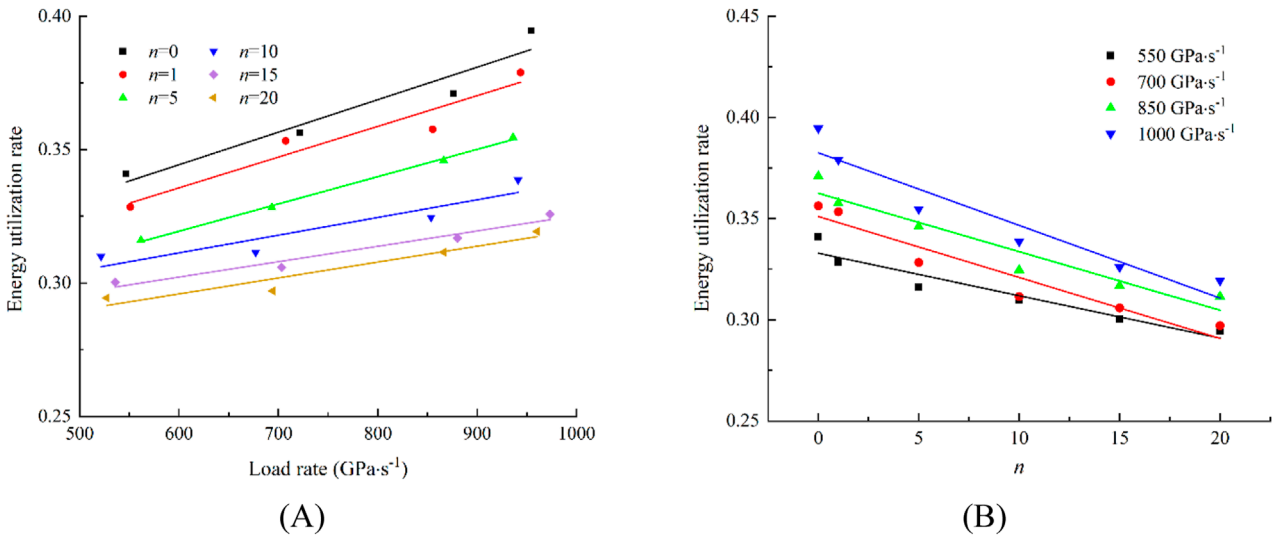

FIGURE 16
Change law of dynamic tensile energy utilization rate of limestone **(A)** Change of energy utilization rate with loading rate (n = 0), **(B)** The change of energy utilization rate with the number of dry and wet cycles (1,000 GPa·s^{-1}).

intensity and environmental preconditioning. The strain-rate hardening effect, induced by higher loading rates, enhances the material's ability to absorb and dissipate energy through increased deformation and fracture activity. On the other hand, the cyclic damage resulting from repeated dry-wet cycles weakens the material structure, making it more prone to energy reflection rather than dissipation. This complex interaction between loading rate and environmental conditioning plays a crucial role in determining the overall energy efficiency of the limestone specimens under dynamic loading.

Figure 17 delineates the dependence of dissipated energy density (ξ_S) on loading rate and wet-dry cycles. As shown in Figure 17A, ξ_S exhibits a linear increase with loading rate; however, cyclic preconditioning reduces strain-rate sensitivity, evidenced by a 22% slope reduction in fitted curves for n = 20 compared to pristine specimens (n = 0). Figure 17B quantifies this degradation: at 0.15 MPa impact pressure, ξ_S declines from 0.337 J·cm^{-3} (n = 0) to 0.275 J·cm^{-3} (n = 20), marking a progressive reduction of 4.15% (n = 1), 10.09% (n = 5), 13.95% (n = 10), 14.24% (n = 15), and 18.40% (n = 20). This trend arises as cyclic hydration-dehydration

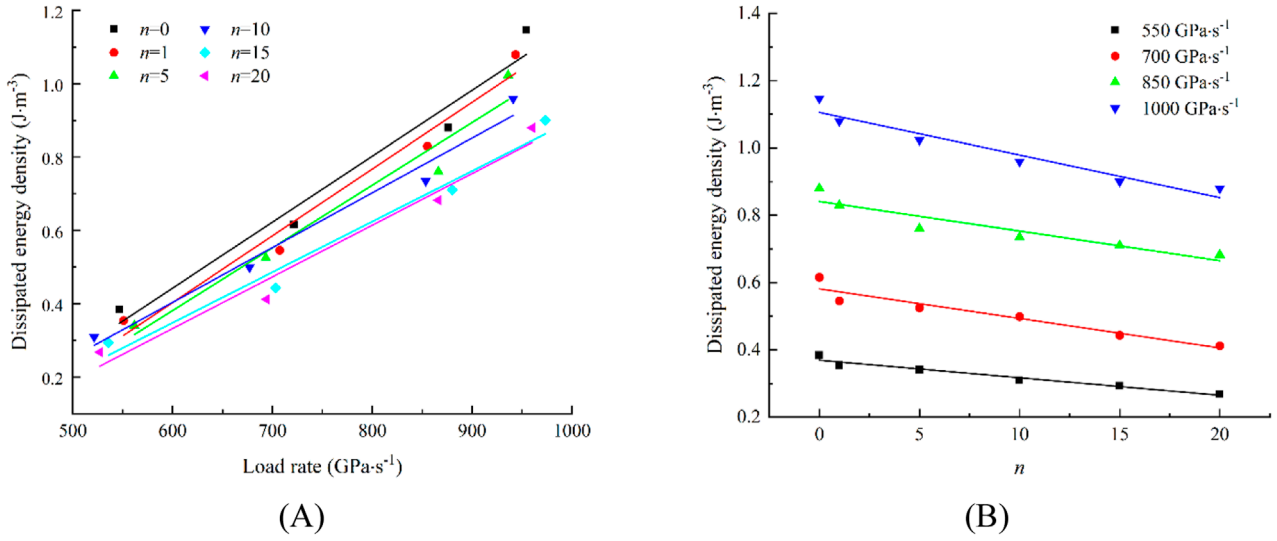

FIGURE 17
Change law of dissipation energy density of limestone **(A)** Change of dissipation energy density with loading rate (n = 0), **(B)** The change of dissipation energy density with the number of dry and wet cycles (1,000 GPa·s^{-1}).

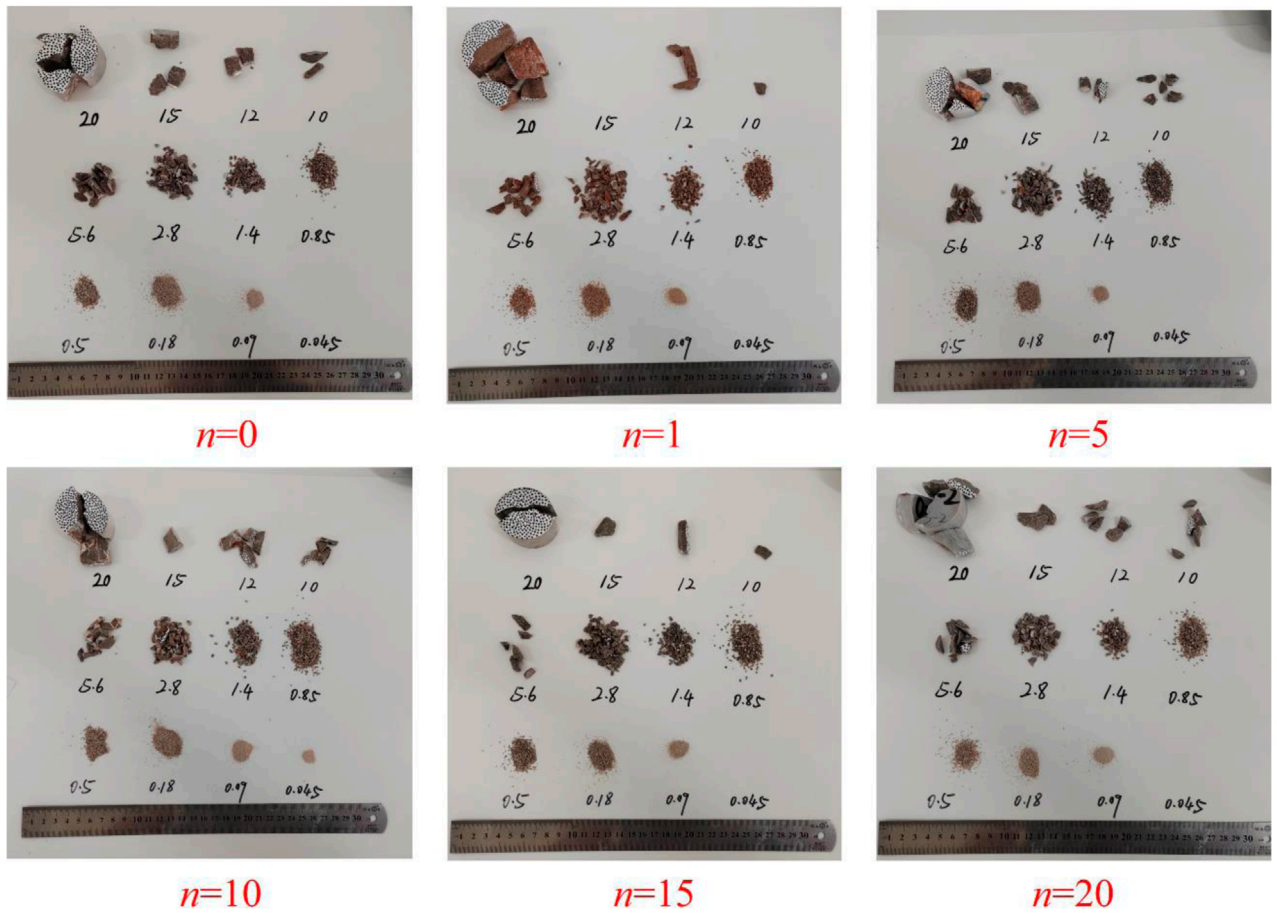

FIGURE 18
Results of rock-like debris sieve screening (0.3 MPa).

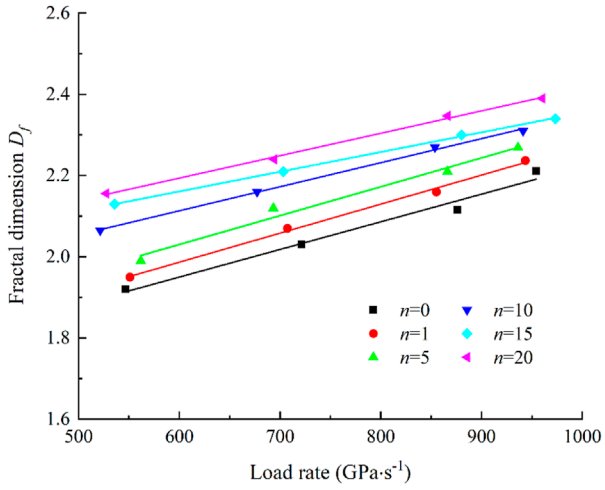

FIGURE 19
The fractal dimension varies with the loading rate.

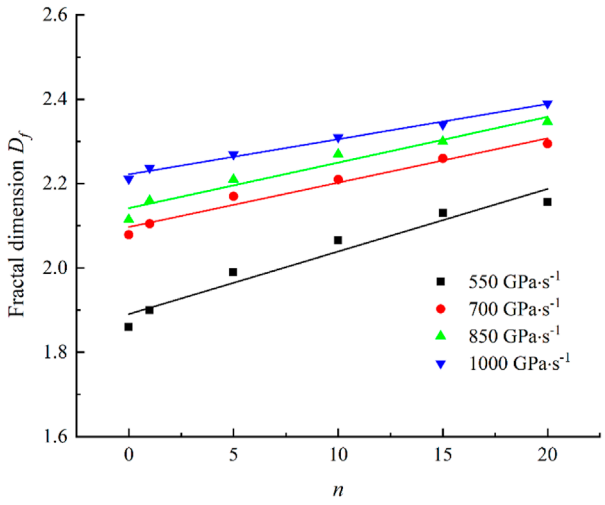

FIGURE 20
The fractal dimension varies with the number of dry-wet cycles.

deteriorates intergranular cohesion, lowering the specimen's load-bearing capacity and energy absorption threshold. Consequently, cyclically weakened specimens' fracture prematurely under reduced energy inputs, suppressing ξ_S.

3.4 Fractal characteristics analysis

The fragment size distribution of dynamically loaded limestone provides direct insights into its stress state and damage evolution, serving as a key indicator for assessing mechanical behavior (Pan et al., 2024; Zhang et al., 2024). Specifically, under blasting or impact conditions, this distribution encapsulates both energy dissipation patterns during fracture and indirect evidence of internal crack initiation, propagation, and coalescence (Feng et al., 2021). Strain rate critically governs fragmentation mechanisms, while microstructural degradation from wet-dry cycles further modifies dynamic failure patterns and fragment size distributions. To systematically characterize tensile fragmentation under varying loading pressures, standard sieve analysis (apertures: 0.045–20 mm) was employed to quantify fragment sizes in cyclically treated limestone. Figure 18 presents the particle size distributions for specimens subjected to 0.3 MPa hydraulic impact pressure across multiple wet-dry cycles, revealing how cyclic preconditioning shifts comminution efficiency and fracture network complexity.

Figure 19 delineates the strain-rate dependency of fragmentation fractal dimensions in limestone under varying wet-dry cycles. The fractal dimension exhibits a linear increase with loading rate, rising from 1.86 at 550 GPa·s^{-1} to 2.21 at 1,000 GPa·s^{-1} for untreated specimens (n = 0). This trend reflects enhanced energy absorption at higher loading rates, which activates more microcracks compared to baseline conditions, intensifying fragmentation complexity. Cyclically treated specimens follow similar linear scaling but with reduced slopes (e.g., 5.518×10^{-4} vs. 6.804×10^{-4} for n = 20 vs. n = 0), indicating diminished strain-rate sensitivity due to pre-existing damage. The relationship is quantified by Equation 10:

$$\begin{cases} D_f = 1.542 + 6.804 \times 10^{-4}\dot{\sigma} & R^2 = 0.979 \quad (n = 0) \\ D_f = 1.558 + 7.175 \times 10^{-4}\dot{\sigma} & R^2 = 0.997 \quad (n = 1) \\ D_f = 1.604 + 7.108 \times 10^{-4}\dot{\sigma} & R^2 = 0.982 \quad (n = 5) \\ D_f = 1.758 + 5.921 \times 10^{-4}\dot{\sigma} & R^2 = 0.998 \quad (n = 10) \\ D_f = 1.870 + 4.848 \times 10^{-4}\dot{\sigma} & R^2 = 0.999 \quad (n = 15) \\ D_f = 1.863 + 5.518 \times 10^{-4}\dot{\sigma} & R^2 = 0.997 \quad (n = 20) \end{cases} \tag{10}$$

where D_f is the fractal dimension, and $\dot{\sigma}$ is the loading rate (GPa·s^{-1}).

The fitted curves reveal a systematic pattern: increasing wet-dry cycles reduce the slope while elevating the intercept (Figure 20; Equation 11). This dual trend signifies that although limestone's fragmentation fractal dimension continues to rise with cyclic damage, its strain-rate sensitivity becomes progressively attenuated. Under constant impact pressure, fractal dimensions increase by 7.7%–15.9% across 0–20 cycles, demonstrating cumulative microstructural degradation. Concurrently, higher loading rates amplify fractal dimensions, but cyclic preconditioning diminishes this rate dependence–slopes decrease by 46.7% with successive cycles. These trends reflect the irreversible deterioration of limestone's physico-mechanical properties under cyclic environmental exposure. While damage accumulates monotonically, its progression rate decelerates, evidenced by the asymptotic stabilization of fractal dimension growth beyond 15 cycles. This nonlinear behavior underscores the saturation of cyclic damage effects, where pre-existing microcracks dominate fragmentation mechanisms, limiting further sensitivity to environmental or mechanical perturbations.

$$\begin{cases} D_f = 1.891 + 0.015n & R^2 = 0.952 \quad (P = 550GPa \cdot s^{-1}) \\ D_f = 2.097 + 0.011n & R^2 = 0.973 \quad (P = 700GPa \cdot s^{-1}) \\ D_f = 2.142 + 0.011n & R^2 = 0.961 \quad (P = 850GPa \cdot s^{-1}) \\ D_f = 2.222 + 0.008n & R^2 = 0.988 \quad (P = 1000GPa \cdot s^{-1}) \end{cases} \tag{11}$$

4 Conclusion

This study investigates the impact of wet-dry cycling on the dynamic mechanical properties of limestone. Dynamic impact loading experiments were conducted under various loading rates and wet-dry cycle conditions using the SHPB system. By combining DIC technology and fractal analysis, the study provides an in-depth analysis of the dynamic tensile strength, crack propagation behavior, strain field evolution, and energy dissipation mechanisms of limestone. The dynamic failure characteristics and underlying mechanisms of limestone under wet-dry cycling were systematically clarified. The key conclusions are as follows:

(1) A significant positive correlation was observed between the loading rate and the dynamic tensile strength of limestone. As the loading rate increased, the tensile strength of the specimens noticeably increased. However, wet-dry cycling weakened the overall mechanical performance of the specimens, reducing their dynamic tensile strength and diminishing their sensitivity to loading rate changes. This indicates that wet-dry cycling degrades the microstructure of the rock, lowering its resistance to failure.

(2) During dynamic impact loading, a strain concentration band initially formed at the center of the specimen, extending along the diameter until it ultimately propagated and formed a primary crack. Wet-dry cycling significantly increased the complexity of crack propagation, enhancing the interaction between primary and secondary cracks. The failure mode gradually shifted from simple splitting to the co-occurrence of multiple cracks, ultimately leading to a higher degree of fragmentation and breakage.

(3) Increasing the loading rate significantly enhanced the incident energy, reflected energy, transmitted energy, and dissipated energy of the limestone specimens, with the dissipated energy showing the fastest growth. This suggests that dynamic failure characteristics of the specimens are more pronounced at higher loading rates. Wet-dry cycling led to a reduction in rock wave impedance, resulting in an increase in reflected energy and a decrease in dissipated energy, indicating that wet-dry cycling weakens the rock's ability to absorb energy and resist failure.

(4) The fractal dimension of fragmentation in limestone increased linearly with the loading rate, suggesting that more micro-cracks participated in the failure process. Wet-dry cycling significantly increased the fractal dimension, but its growth rate gradually slowed as the number of cycles increased. Additionally, after multiple cycles, crack propagation exhibited obvious multi-scale features, indicating that the rock's porosity and the complexity of the crack network significantly impacted the failure mode.

Data availability statement

The original contributions presented in the study are included in the article/supplementary material, further inquiries can be directed to the corresponding author.

Author contributions

WD: Writing–original draft. PG: Conceptualization, Formal Analysis, Methodology, Writing–original draft. BC: Formal Analysis, Methodology, Writing–review and editing. CP: Writing–review and editing.

Funding

The author(s) declare that financial support was received for the research, authorship, and/or publication of this article. This work was financially supported by the National Natural Science Foundation of China (No. 52304075), the Foundation of Anhui Engineering Research Center of New Explosive Materials and Blasting Technology (No. AHBP2023A-02), and Anhui Natural Science Foundation (2408085QA029).

Conflict of interest

Authors WD and PG were employed by Anhui Jiangnan Chemical Industry Co., Ltd.

The remaining authors declare that the research was conducted in the absence of any commercial or financial relationships that could be construed as a potential conflict of interest.

Generative AI statement

The author(s) declare that no Generative AI was used in the creation of this manuscript.

Publisher's note

References

An, R., Kong, L., Zhang, X., and Li, C. (2022). Effects of dry-wet cycles on three-dimensional pore structure and permeability characteristics of granite residual soil using X-ray micro computed tomography. *J. Rock Mech. Geotech.* 14 (3), 851–860. doi:10.1016/j.jrmge.2021.10.004

Cai, X., Zhou, Z., Tan, L., Zang, H., and Song, Z. (2020). Fracture behavior and damage mechanisms of sandstone subjected to wet-ting-drying cycles. *Eng. Fract. Mech.* 234, 107109. doi:10.1016/j.engfracmech.2020.107109

Feng, P., Xu, Y., and Dai, F. (2021). Effects of dynamic strain rate on the energy dissipation and fragment characteristics of cross-fissured rocks. *Int. J. Rock Mech. Min.* 138, 104600. doi:10.1016/j.ijrmms.2020.104600

Gao, P., Pan, C., Zong, Q., and Dong, C. (2023). Rock fragmentation size distribution control in blasting: a case study of blasting mining in Changjiu Shenshan limestone mine. *Front. Mater.* 10, 1330354. doi:10.3389/fmats.2023.1330354

Guo, P., Gu, J., Su, Y., Wang, J., and Ding, Z. (2021). Effect of cyclic wetting–drying on tensile mechanical behavior and microstructure of clay-bearing sandstone. *Int. J. Coal Sci. Technol.* 8, 956–968. doi:10.1007/s40789-020-00403-3

He, R., Tang, X., Yin, H., Qin, Y., Guo, Z., Fang, L., et al. (2024). Investigating the impact of the quantity of wet and dry cycles on the mechanical characteristics and fracture variations of sandstones. *Sci. Rep.* 14, 13278. doi:10.1038/s41598-024-63577-9

Hua, W., Dong, S., Li, Y., and Wang, Q. (2016). Effect of cyclic wetting and drying on the pure mode II fracture toughness of sandstone. *Eng. Fract. Mech.* 153, 143–150. doi:10.1016/j.engfracmech.2015.11.020

Jorge, Z., Ronny, P., and Sotomayor, O. (2022). On the digital image correlation technique. *Mater. Today Proc.* 49, 79–84. doi:10.1016/j.matpr.2021.07.476

Khanlari, G., and Abdilor, Y. (2015). Influence of wet–dry, freeze–thaw, and heat–cool cycles on the physical and mechanical properties of Upper Red sandstones in central Iran. *Bull. Eng. Geol. Environ.* 74 (4), 1287–1300. doi:10.1007/s10064-014-0691-8

Li, J. (2013). Wave propagation across non-linear rock joints based on time-domain recursive method. *Geophys. J. Int.* 193 (2), 970–985. doi:10.1093/gji/ggt020

Li, J., Li, H., Jiao, Y., Liu, Y., Xia, X., and Yu, C. (2014). Analysis for oblique wave propagation across filled joints based on thin-layer interface model. *J. Appl. Geophys.* 102, 39–46. doi:10.1016/j.jappgeo.2013.11.014

Li, J., Li, N., Li, H., and Zhao, J. (2017). An SHPB test study on wave propagation across rock masses with different contact area ratios of joint. *Int. J. Impact Eng.* 105, 109–116. doi:10.1016/j.ijimpeng.2016.12.011

Luo, Y., Huang, J., Si, X., Wu, W., and Li, S. (2025). Failure characteristics and energy properties of red sandstone under uniaxial compression: water content effect and its application. *B. Eng. Geol. Environ.* 84, 57. doi:10.1007/s10064-025-04085-6

Meng, B., Jing, H., Zhu, W., and Su, H. (2019). Influences of saturation and wetting–drying cycle on mechanical performances of argillaceous limestones from liupanshan tunnel, China. *Adv. Mater. Sci. Eng.* 2019, 1–10. doi:10.1155/2019/9236172

Pan, C., Li, X., Zhao, G., and Cheng, B. (2025). Effect of mesostructure on quasi-static and dynamic tensile strength of rock: insights from a breakable grain-based model. *Geomech. Geophys. Geo-energ. Geo-resour.* 11, 2. doi:10.1007/s40948-024-00916-0

Pan, C., Liu, C., Zhao, G., Yuan, W., Wang, X., and Meng, X. (2024). Fractal characteristics and energy evolution analysis of rocks under true triaxial unloading conditions. *Fractal Fract.* 8 (7), 387. doi:10.3390/fractalfract8070387

Pan, C., Xie, L., Li, X., Liu, K., Gao, P., and Tian, L. (2022). Numerical investigation of effect of eccentric decoupled charge structure on blasting-induced rock damage. *J. Cent. South Univ.* 29, 663–679. doi:10.1007/s11771-022-4947-3

Pu, H., Yi, Q., Jivkov, A. P., Bian, Z., Chen, W., and Wu, J. (2024). Effect of dry-wet cycles on dynamic properties and microstructures of sandstone: experiments and modelling. *Int. J. Min. Sci. Techno.* 34, 655–679. doi:10.1016/j.ijmst.2024.04.008

Qiu, J., Xie, H., Zhu, J., Wang, J., and Deng, J. (2023b). Dynamic response and rockburst characteristics of underground cavern with unexposed joint. *Int. J. Rock Mech. Min.* 169, 105442. doi:10.1016/j.ijrmms.2023.105442

Qiu, J., Zhou, C., Wang, Z., and Feng, F. (2023a). Dynamic responses and failure behavior of jointed rock masses considering pre-existing joints using a hybrid BPM-DFN approach. *Comput. Geotech.* 155, 105237. doi:10.1016/j.compgeo.2022.105237

Rueden, C. T., Schindelin, J., Hiner, M. C., DeZonia, B. E., Walter, A. E., Arena, E. T., et al. (2017). ImageJ2: ImageJ for the next generation of scientific image data. *BMC Bioinforma.* 18, 529–626. doi:10.1186/s12859-017-1934-z

Xu, J., Sun, H., Cui, Y., Fei, D., Lan, H., Yan, C., et al. (2021). Study on dynamic characteristics of diorite under dry–wet cycle. *Rock Mech. Rock Eng.* 54 (12), 6339–6349. doi:10.1007/s00603-021-02593-x

Zhang, H., Lu, K., Zhang, W., Li, D., and Yang, G. (2022). Quantification and acoustic emission characteristics of sandstone damage evolution under dry–wet cycles. *J. Build. Eng.* 48, 103996. doi:10.1016/j.jobe.2022.103996

Zhang, Q., Meng, X., and Zhao, G. (2024). Energy evolution and fractal characteristics of sandstones under true triaxial cyclic loading and unloading. *Fractal Fract.* 8 (12), 714. doi:10.3390/fractalfract8120714

Zhou, Y., Zou, S., Wen, J., and Zhang, Y. (2023). Study on the damage behavior and energy dissipation characteristics of basalt fiber concrete using SHPB device. *Constr. Build. Mater.* 368, 130413. doi:10.1016/j.conbuildmat.2023.130413

Zhou, Y. X., Xia, K., Li, X. B., Li, H. B., Ma, G. W., Zhao, J., et al. (2012). Suggested methods for determining the dynamic strength parameters and mode-I fracture toughness of rock materials. *Int. J. Rock Mech. Min. Sci.* 49, 105–112. doi:10.1016/j.ijrmms.2011.10.004